

Molecular dynamics simulation of the interaction of a nano-scale crack with grain boundaries in α -Fe



A. Kedharnath^{a,b}, Ajay Singh Panwar^a, Rajeev Kapoor^{b,*}

^a Dept of Metallurgical Engineering and Materials Science, Indian Institute of Technology Bombay, Mumbai 400 076, India

^b Mechanical Metallurgy Division, Bhabha Atomic Research Centre, Mumbai 400 085, India

ARTICLE INFO

Article history:

Received 21 March 2017

Received in revised form 12 May 2017

Accepted 13 May 2017

Available online 26 May 2017

Keywords:

Molecular dynamics simulation

Symmetric tilt grain boundary

Grain boundary crack interaction

ABSTRACT

The interaction of nano-scale cracks with grain boundaries in α -Fe were studied using symmetric tilt grain boundaries with $[112]$ and $[110]$ tilt axis. For each tilt axis four types of grain boundaries were chosen – low angle, general high angle, $\Sigma 3$ and $\Sigma 11$. A crack perpendicular to the boundary plane was introduced between the two boundaries. The grain boundaries were equilibrated using molecular statics simulation and the entire configuration was deformed at constant strain rate using isobaric-isothermal (NPT) ensemble at 0 K. The stress strain behaviour of the configurations, variation of dislocation line density with strain and the screening effect of the grain boundaries were studied. The strain field around the crack tip and the dislocations emitted from it interact with the grain boundaries. The configuration with $\Sigma 3$ grain boundaries showed higher tensile strength while that with $\Sigma 11$ showed lower tensile strength. This was attributed to the orientation of the dislocations in the $\{1\bar{1}0\}$ boundary plane with 180° tilt angle and the complete coherency with $\{1\bar{1}2\}$ boundary plane with 70.53° tilt angle. Further, in both the $\Sigma 3$ grain boundary configurations, even the most favourable slip system had a low Schmid factor, thus making slip difficult in the grain too. The configurations with 4.9° and 31.59° tilt angle about the $[110]$ tilt axis showed the most effective stress screening.

© 2017 Elsevier B.V. All rights reserved.

1. Introduction

Grain boundaries act as barriers for dislocation movement resulting in dislocation pile-up thereby strengthening the material. Grain boundaries are surface defects and can be thought of as being created when two grains are tilted, twisted, twinned or mixed with respect to each other. They can be classified on the basis of misorientation angle φ as low angle ($\varphi < 15^\circ$) and high angle ($\varphi > 15^\circ$) grain boundaries. Low angle grain boundaries are made up of arrays of dislocations, the number of which increases with φ from 0° to 15° , which in turn results in an increase in the grain boundary energy [1]. For $\varphi > 15^\circ$, the dislocation cores start to overlap, making the boundary dislocations lose their identity. Beyond this, the grain boundary energy may not increase with further increase in the misorientation angle. Apart from these general high angle boundaries there exists special high angle grain boundaries, referred to as coincidence site lattice (CSL) or sigma boundaries, in which some lattice points of the two crystals coincide resulting in a significantly lower grain boundary energy [1]. Symmetric tilt grain boundaries have equal but opposite tilt angle of two grains

about a common tilt axis. The variation of grain boundary energy with tilt angle depends on the tilt axis the material [2,3].

Grain boundaries influence the deformation behaviour of materials in various ways. Apart from acting as barriers to the motion of dislocations, they could also interact with voids [4] and cracks [5–7] during the process of fracture. The stress field around the crack tip could result in emission of dislocations which would then interact with grain boundaries and result in a mechanical response different from that without cracks [5,8,9].

Experiments to study the influence of grain boundaries on deformation and fracture at nano-scale can be costly and time consuming. As the specimen thickness is reduced for TEM investigation, the grain boundary structure may relax and change [10]. Thus the experimental observation of dislocation nucleation, movement and interaction with grain boundaries are difficult. Computational modelling has played an important role in understanding the interaction of grain boundaries with dislocations and cracks. Taira et al. [11] modeled a micron sized slip band near the crack tip whose formation was affected by the grain boundary near them. The model was used for fatigue crack growth [11], microcrack propagation in brittle material [12] and its interaction with grain boundary [13] under fatigue loading [6]. Of the different computational methods, molecular dynamics (MD) simulation is

* Corresponding author.

E-mail address: rk Kapoor@barc.gov.in (R. Kapoor).

an useful tool to study the mechanical response of materials at different temperatures [14], strain rates and loading conditions [15]. Molecular dynamics simulation along with experiments can give a better understanding of the crack propagation at the atomic scale [16]. Researchers have used molecular dynamics to study the mechanical behaviour of fcc and bcc materials containing voids, cracks and grain boundaries under tensile and fatigue loading conditions. Molecular dynamics simulations of the tensile behaviour of platinum, gold, rhodium and silver at different temperatures showed the failure to be due to void and nano-crack formation [17]. Grain boundary as a dislocation source in nanocrystalline Cu under tensile loading [18] and with vacancies under cyclic loading [19] were studied using MD. The fracture mechanism of bcc metals such as V, Nb, Mo, Ta, and W [4], intergranular and intragranular fracture in nanocrystalline iron [20], and crack growth under cyclic loading in α -Fe [21] have also been studied using MD.

Of the various research articles on crack or dislocation interaction with grain boundaries [22,23] most are related to fcc materials [17–19,24]. As the use of bcc materials in engineering applications is extensive, an understanding of boundary-crack-dislocation interaction is essential for designing new grain boundary engineered alloys. The motivation of the present work was to use molecular dynamics simulations to study the interaction of a crack (and the dislocations emitted from it) with symmetric tilt grain boundaries in α -Fe. Low and high angle grain boundaries, $\Sigma 3$ and $\Sigma 11$ boundaries, having a tilt axis of $[11\bar{2}]$ and $[\bar{1}10]$ were chosen for this study. The relative strength of all the grain boundary configurations of both tilt axes was compared.

2. Simulation methodology

2.1. Grain boundary model

In symmetric tilt grain boundaries, the tilt and rotation of the crystals are symmetric about a common tilt axis. In this study, two sets of grain boundaries were formed, one with tilt axis $[11\bar{2}]$ and the other with tilt axis $[\bar{1}10]$. For each tilt axis, grain boundaries having different tilt angles between 0° and 180° were selected (each crystal was tilted by 0° – 90°). The $[11\bar{2}]$ tilt axis was selected because of the ease of activation of the $\{110\}(111)$ slip system at low misorientation angles. The $[\bar{1}10]$ tilt axis was selected as this produces a coherent twin boundary. The model consists of three crystals and two grain boundaries with periodic boundary conditions. The central rotated crystal (C-2) is between the other two rotated crystals (C-1 and C-3) as shown in Fig. 1. Prior to rotation of the crystals, the crystallography of the parent crystal for $[11\bar{2}]$ tilt axis, was $[\bar{1}10]$ along x direction, $[111]$ along y direction and $[11\bar{2}]$ along z direction. Similarly, for $[\bar{1}10]$ tilt axis, the parent crystal had $[\bar{1}10]$ along x direction, $[001]$ along y direction and $[\bar{1}10]$ along z direction. A crack perpendicular to the grain boundary plane of 4 \AA thicknesses with crack tips at a distance of 50 \AA from both the grain boundaries was created by deleting atoms in the centre of the crystal C-2. As a comparison to the above mentioned grain boundary–crack configurations, the tensile behaviour of configurations with a perpendicular crack in a single crystal (C-2 in Fig. 1) were also simulated.

2.1.1. Low and high angle grain boundaries

A low angle grain boundary (LAGB) can be modeled as an array of edge dislocations. The distance d between the two dislocations with magnitude of Burgers vector b for a tilt angle 2θ (radian) is given by the relation

$$\frac{b}{d} = 2 \sin(\theta) \approx 2\theta \quad (\text{for small tilt angle}) \quad (1)$$

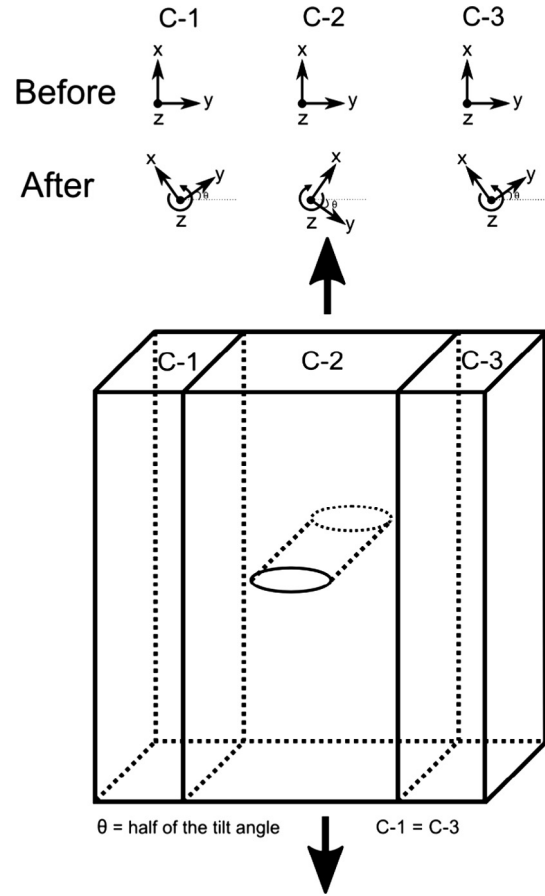


Fig. 1. Schematic image of the grain boundary–crack tensile model. Three rotated crystals C-1, C-2 and C-3 in which C-1 is similar to C-3 in rotation. θ is half of the tilt angle.

The x-dimension of the simulation box was chosen to get the required number of dislocations in the grain boundary region (16 dislocations in $[11\bar{2}]$ tilt axis LAGB and 12 dislocations in $[\bar{1}10]$ tilt axis LAGB). With increasing 2θ , d decreases and the number of dislocation per unit area increases, thus increasing the grain boundary energy. For tilt angles $>15^\circ$, individual dislocations are not distinguishable as their cores overlap and their grain boundary energy does not necessarily increase.

2.1.2. Coincidence site lattice

For certain tilt angles, coincidence site lattice (CSL) boundaries form where some lattice sites of one crystal coincide with that of the other crystal. The elementary cell of any CSL is bigger than that of the crystal and can be quantified by the parameter Σ which is the ratio of the volume of elementary cell of CSL to the volume of elementary cell of the crystal. For every tilt angle, the volume of elementary cell of crystal and CSL varies and so does Σ [18]. Ranganathan gave a relation between the tilt angle 2θ , tilt axis $[uvw]$ and Σ for cubic crystal [25],

$$\tan(\theta) = \frac{n * (u^2 + v^2 + w^2)^{\frac{1}{2}}}{m} \quad (2)$$

$$S = m^2 + n^2 * (u^2 + v^2 + w^2) \quad (3)$$

$$S = \alpha \sum \quad (4)$$

where m and n are integers; and α must be either 1 or 2 or 3; and S is an odd factor. The directions of the rotated crystals were found

using the above formula when the parent crystals are rotated by $\pm\theta$ (total tilt angle is 2θ) about the tilt axis.

2.2. Grain boundary energy minimization

The grain boundary model as described in Section 2.1 was created by modifying Tschopp's LAMMPS [26] script using molecular statics technique [27]. From the various potentials available in literature for Fe [28–30], values of different properties, such as cohesive energy, lattice parameter and elastic constants were calculated and compared with those in literature [31]. Of the various potentials, the embedded atom model (EAM) potential by Ackland [28] was found to give the closest values of the properties when compared to that in literature. The values of different properties calculated using the selected potential are: cohesive energy (eV) = -4.32 ; lattice parameter (\AA) = 2.867 ; elastic constants (GPa) $C_{11} = 243.418$, $C_{12} = 145.06$, $C_{44} = 116.028$. The grain boundary energy (γ_{gb}) was minimized by the following procedure: crystal C-2 was translated incrementally in both x and z directions in the grain boundary plane with respect to both C-1 and C-3, and γ_{gb} was calculated using the potential energy (E_p), cohesive energy (E_c) and the area of the grain boundary (A_{gb}) with n number of atoms using

$$\gamma_{gb} = \frac{E_p - (nE_c)}{A_{gb}} \quad (5)$$

This procedure was repeated until the grain boundary energy reached a global minimum. The minimum grain boundary energy corresponded to the most stable configuration of atoms for that particular tilt angle. The grain boundary plane, their corresponding tilt angle and grain boundary energy of different grain boundaries with $[1\bar{1}2]$ and $[\bar{1}10]$ tilt axis are tabulated in Appendix Tables A1 and A2 respectively. The average number of atoms used in the simulation was 6×10^5 with approximate simulation box dimensions as 300 \AA , 300 \AA and 70 \AA .

2.3. Deformation and dislocation extraction

The stress strain behaviour of the interaction of a crack with different types of grain boundaries was studied. For this, few equilibrated grain boundaries were selected from each tilt axis – a low angle grain boundary, a high angle grain boundary, and two CSL grain boundaries $\Sigma 3$ and $\Sigma 11$ based on classification (see Sections 2.1.1 and 2.1.2). The system was equilibrated at 0 K for 1 ps (picosecond) using Nose-Hoover thermostat. The simulation box was deformed by displacement control at a constant strain rate of 10^{11} s^{-1} along x dimension. The pressure at the other two axes (y and z direction) were made zero after every deformation step. The isobaric-isothermal (NPT) ensemble was used during the deformation. The deformation was run for 20 ps till a strain of 0.2. Pressure, temperature and change in dimensions were calculated during deformation for every 100 fs (femtosecond). The atom's configurations during deformation were dumped to a file which was later visualized using OVITO (Open Visualization Tool) [29]. The stress was calculated at every timestep and plotted against strain. The dislocations and their line density were extracted from the crystal using the dislocation extraction algorithm (DXA) in Crystal Analysis Tool (CATool) [30]. The deformation twins were visualized near the crack tip using common neighbor analysis (CNA). Using CNA, the perfect bcc atoms were colored blue, bcc atoms that deformed to form hcp and fcc were colored red and green respectively, other atoms whose structure was neither bcc, fcc nor hcp were colored white. Deformation twins have the same crystal structure as the parent but are oriented differently.

2.4. Stress screening effect

The stress field due to a crack in crystal C-2 may not be completely seen by crystal C-1 due to the presence of the grain boundary (C-1, C-2 shown in Fig. 1). The grain boundaries can be said to “screen” the stress field, and this phenomenon can be referred to as the “screening” effect of grain boundaries. In order to see the effect of the grain boundary on the screening of the stress field due to a crack, the stress at two locations – one near the crack in crystal C-2 and other in the crystal C-1 were determined as shown in Fig. 2. Points a , b , a' and b' lie in the crack plane. b represents the position near the grain boundary. b is 5 \AA for the low angle and $\Sigma 3$ grain boundary configurations and 10 \AA for the high angle and $\Sigma 11$ grain boundary configurations. They were different for different configurations because of the different grain boundary structure and grain boundary thickness for different grain boundaries. a represents a position near the crack tip at the same distance which b was from the grain boundary. a' and b' are the corresponding positions in the single crystal configurations. The position of a' and b' are same as that of a and b . From LAMMPS, value of the stress per atom was obtained as ' $\sigma_{xx} \times V_{atom}$ ', where σ_{xx} is the normal stress component along x direction in GPa and V_{atom} is the volume of an atom in \AA^3 . To map the stress field, summation of stress per atom values of few layers of atoms in a volume of ' $10 \text{ \AA} \times 10 \text{ \AA} \times \text{layer thickness}$ ' was calculated. The stress used for mapping ($\sigma_{mapping}$) is obtained by dividing the summation value by the volume of the layer considered.

$$\sigma_{mapping} = \frac{\sum \sigma_{xx} * V_{atom}}{\text{Volume of the layer of atoms}} \quad (6)$$

The stress mapping was done at every timestep. The effectiveness of stress screening by the grain boundary can be studied by determining the ratio of stress in C-1 at b to that in C-2 at a , i.e. $\frac{\sigma_b}{\sigma_a}$ and comparing with the corresponding ratio for the single crystal, which is $\frac{\sigma_{b'}}{\sigma_{a'}}$. The plot of these ratios with strain gives an estimate of the stress screening by the grain boundary.

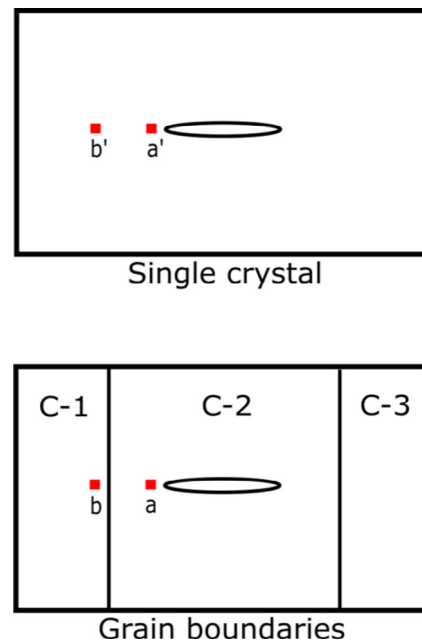


Fig. 2. Model used for studying stress screening effect by the grain boundary. The point b is away from grain boundary (about $5\text{--}10 \text{ \AA}$ depending on configuration) and the point a is at same distance from the crack tip. b' and a' are the corresponding points in the single crystal. In single crystal, b' is away from a' by the same distance as b is away from a .

3. Results

This section presents the results of the simulation of the different grain boundary–crack configurations as described in the earlier section (a low angle and general high angle grain boundaries and two CSL boundaries from each of the tilt axis). The results include (1) the minimized grain boundary energy as a function of tilt angle for both $[11\bar{2}]$ and $[\bar{1}10]$ tilt axis, (2) the stress strain behaviour, (3) maximum tensile stress as a function of tilt angle, (4) schmid factor of different slip systems near the crack, (5) visualization of dislocations and deformation twins, (6) variation of dislocation line density with strain, (7) stress mapping and stress screening effect.

3.1. Grain boundary energy vs. tilt angle

Fig. 3 shows the variation of grain boundary energy as a function of tilt angle for $[11\bar{2}]$ and $[\bar{1}10]$ tilt axis grain boundaries. The corresponding grain boundary energy values are listed in Tables A1 and A2 in Appendix. Here, grain boundaries are represented using the format “tilt angle grain boundary plane” for low angle and general high angle boundaries, and “tilt angle sigma grain boundary plane” for CSL grain boundaries. For example, $180^\circ \Sigma 3 \{1\bar{1}0\}$ represents a grain boundary with 180° as the tilt angle, $\Sigma 3$ as the CSL/sigma boundary and $\{1\bar{1}0\}$ as the grain boundary plane. Other boundaries are also represented according to this nomenclature. It is seen from Fig. 3 that both $180^\circ \Sigma 3 \{1\bar{1}0\}$ and $70.53^\circ \Sigma 3 \{\bar{1}\bar{1}2\}$ have low grain boundary energies due to their coincidence site lattices in the grain boundaries. The energy of the low angle grain boundary comes from the array of dislocations in grain boundary region. Increasing the tilt angle increases the number of dislocations thus increasing the grain boundary energy. The energy profile of $[11\bar{2}]$ and $[\bar{1}10]$ tilt axis grain boundaries are nearly similar (Fig. 3). The variation of grain boundary energy as a function of tilt axis for $[\bar{1}10]$ tilt axis is similar to that of the $\langle 110 \rangle$ tilt axis grain boundary of iron as shown in Ref. [3]. The different grain boundary structures from top and perspective view are shown in Fig. 4. This is obtained as follows – first the atoms in the grain boundary regions are identified using

common neighbor analysis (CNA), then the perfect bcc atoms are deleted and the remaining atoms are shown in the figure.

3.2. Stress strain behaviour

Fig. 5 shows the stress (σ_{xx}) strain (ϵ_{xx}) behaviour of two types of configurations: grain boundary with a crack perpendicular to the grain boundary (represented by solid lines) and single crystal with a crack (represented by dotted lines). The single crystal with crack configuration was the C-2 crystal without any grain boundary.

For the set of boundaries with $[11\bar{2}]$ tilt axis, the $180^\circ \Sigma 3 \{1\bar{1}0\}$ and $4.92^\circ \{201819\}$ configurations showed high tensile strength. The $180^\circ \Sigma 3 \{1\bar{1}0\}$ configuration had similar stress strain curve for configurations with and without grain boundaries. The $4.92^\circ \{201819\}$ low angle grain boundary configuration had a higher tensile strength than the corresponding single crystal configuration. High angle grain boundary $32.51^\circ \{19914\}$ configuration showed less tensile strength as compared to the corresponding single crystal configuration. $62.96^\circ \Sigma 11 \{714\}$ showed the lowest tensile strength compared to all grain boundary configurations.

For the set of boundaries with $[\bar{1}10]$ tilt axis, the $70.53^\circ \Sigma 3 \{\bar{1}\bar{1}2\}$ configuration showed the highest tensile strength. The tensile behaviour of $70.53^\circ \Sigma 3 \{\bar{1}\bar{1}2\}$ and $4.9^\circ \{\bar{1}\bar{1}33\}$ configurations were similar for both with and without grain boundaries. $129.52^\circ \Sigma 11 \{\bar{3}\bar{3}2\}$ and $31.59^\circ \{\bar{1}\bar{1}5\}$ grain boundaries showed less tensile strength than that of the corresponding single crystal configurations. $129.52^\circ \Sigma 11 \{332\}$ showed the lowest tensile strength.

For both the tilt axes cases, $\Sigma 11$ grain boundary configurations had the lowest tensile strength. In most cases, the tensile strength and the strain hardening of the single crystal configuration were marginally higher than that of the corresponding grain boundary configuration.

3.3. Variation of maximum tensile stress

For the $[11\bar{2}]$ tilt axis configurations, the lower (4.92°) and higher tilt angle ($\Sigma 3$) configurations have higher maximum tensile stress. For the $[\bar{1}10]$ tilt axis configurations the mid tilt angle ($\Sigma 3$)

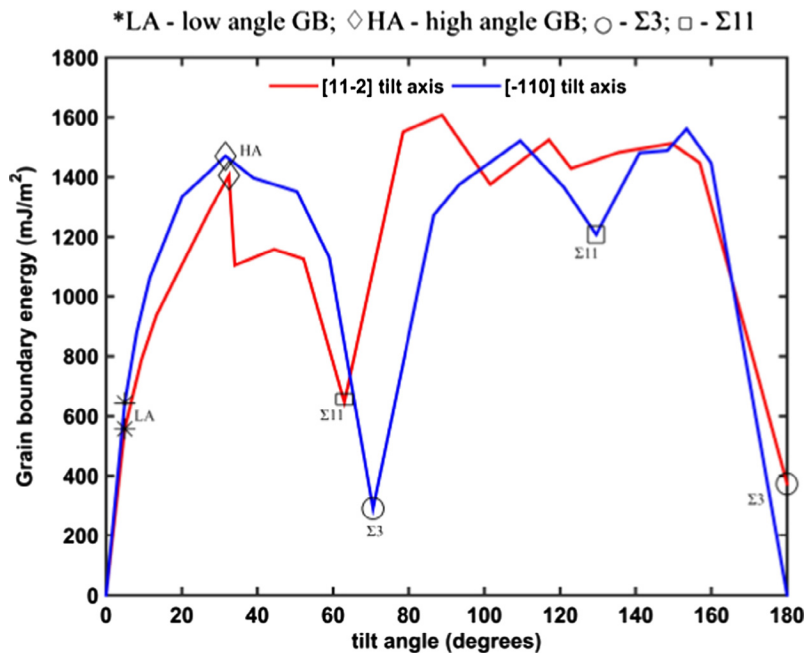


Fig. 3. Variation of grain boundary energy as a function of tilt angle for $[11\bar{2}]$ and $[\bar{1}10]$ tilt axis.

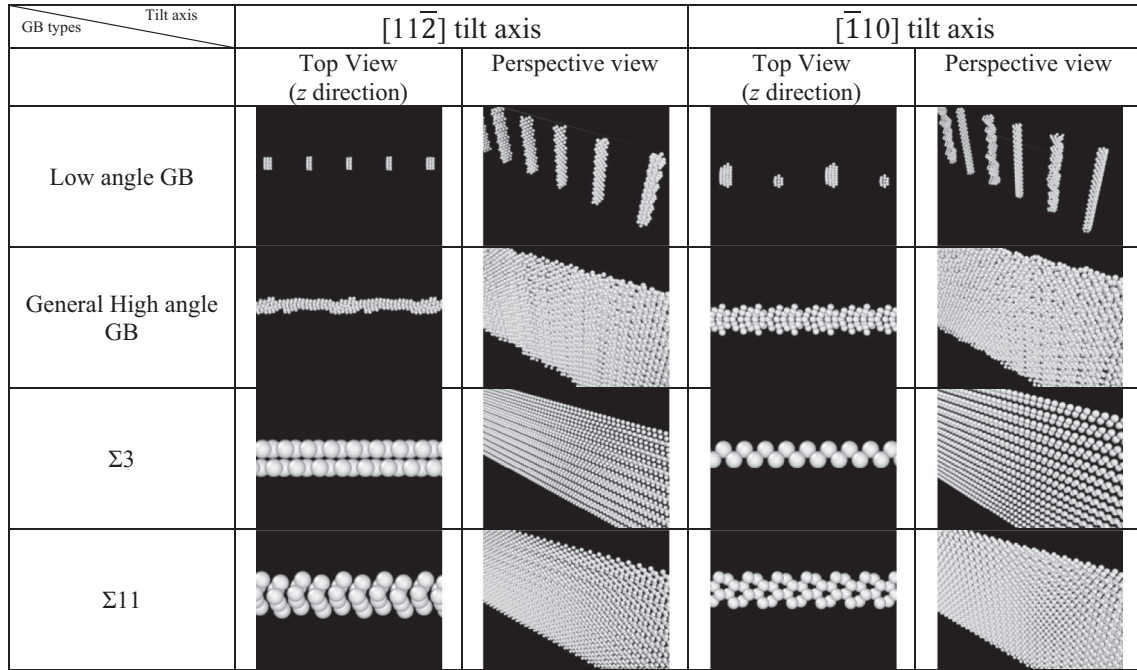


Fig. 4. Grain boundary structure from top and perspective views for [112] and [110] tilt axis grain boundaries.

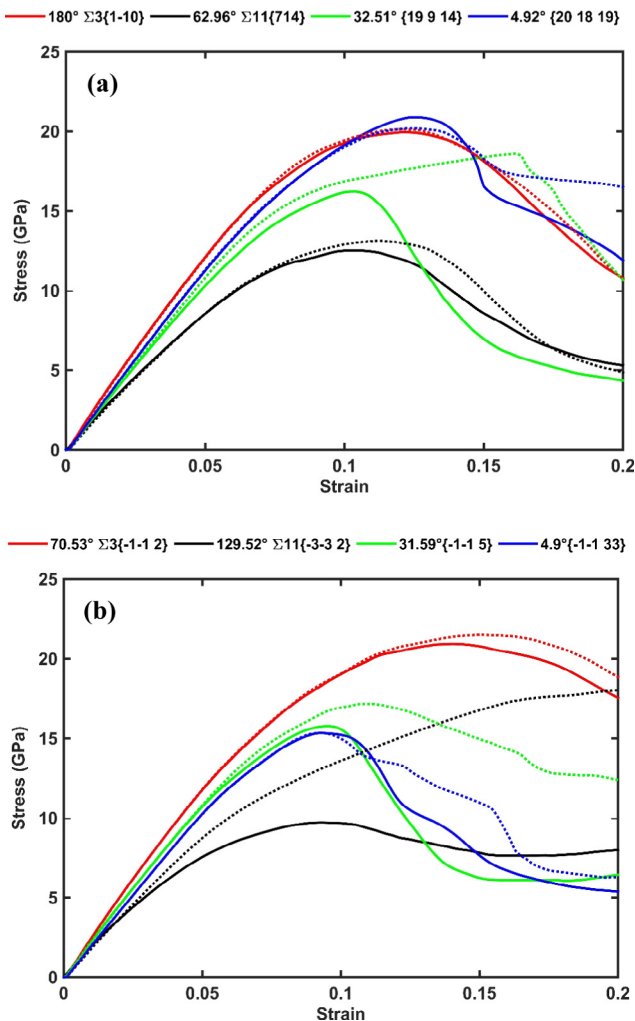


Fig. 5. Stress strain behaviour of different grain boundaries with (a) [112] tilt axis (b) [110] tilt axis. Solid lines represent system with crack perpendicular to the grain boundary plane; dotted lines represent single crystal (C-2 type) with a crack.

has a high maximum tensile stress (Fig. 6). Appendix Tables A1 and A2 list the values of maximum tensile stress of different grain boundaries with [112] and [110] tilt axes, respectively. The 4.92° {20 18 19} low angle configuration of the [112] tilt axis has a high tensile stress due to the presence of $\frac{1}{2}\langle 1\ 1\ 1\rangle$ type of dislocations in the boundary which are unfavourably oriented for slip (Schmid factor is 0.02). The high maximum stress value at the high tilt angle (the 180° $\Sigma 3\{1\ \bar{1}\ 0\}$ configuration) is due to the presence of $\frac{1}{2}\langle 1\ 1\ 1\rangle$ type of dislocations along the grain boundary plane and parallel to the loading direction, which are also unfavorably oriented for slip. The presence of coherent twin boundary 70.53° $\Sigma 3\{\bar{1}\ \bar{1}\ 2\}$ with [110] tilt axis also showed high maximum tensile stress. These results show that $\Sigma 3$ boundary configurations have

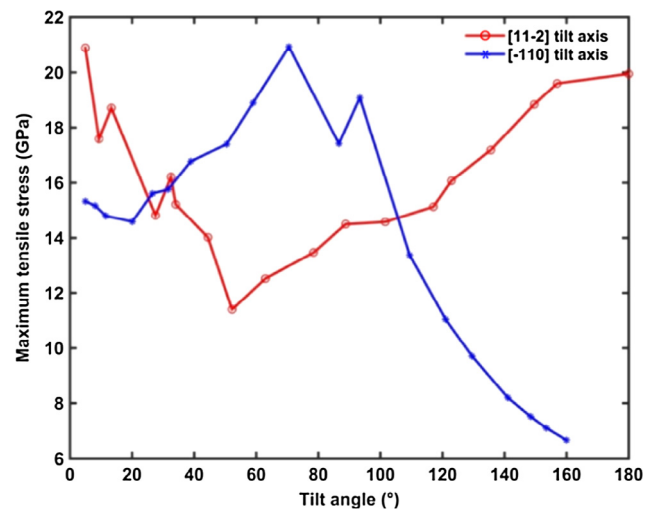


Fig. 6. Variation of Maximum tensile stress as a function of tilt angle for different grain boundaries. Red color represents results from [112] tilt axis grain boundaries; blue color represents results from [110] tilt axis grain boundaries. (For interpretation of the references to color in this figure legend, the reader is referred to the web version of this article.)

Table 1
Simulation results of different selected grain boundaries with slip system with maximum Schmid factor.

Tilt axis	GB type	GBE (mj/m ²)	Tilt angle (°)	Max. tensile stress (GPa)	Loading direction	Slip plane	Slip direction	Schmid factor
[112]	{201819}	557.60	4.92	20.9	[59552]	($\bar{1}12$)	$[\bar{1}11]$	0.479
	{19914}	1405.45	32.51	16.2	$[\bar{2}6165]$	(213)	$[\bar{1}11]$	0.495
	$\Sigma 3$	373.56	180	20.0	$[\bar{1}\bar{1}\bar{1}]$	(211)	$[\bar{1}11]$	0.314
	$\Sigma 11$	646.45	62.96	12.5	$[311]$	(110)	[111]	0.445
$[\bar{1}10]$	$\{\bar{1}\bar{1}33\}$	643.38	4.91	15.3	$[\bar{3}3\bar{3}2]$	(112)	[111]	0.484
	$\{\bar{1}\bar{1}5\}$	1470.44	31.59	15.8	[552]	(112)	[111]	0.489
	$\Sigma 3$	291.41	70.53	20.9	$[\bar{1}\bar{1}1]$	(112)	[111]	0.314
	$\Sigma 11$	1207.83	129.52	9.7	$[\bar{1}\bar{1}3]$	(011)	$[\bar{1}11]$	0.445

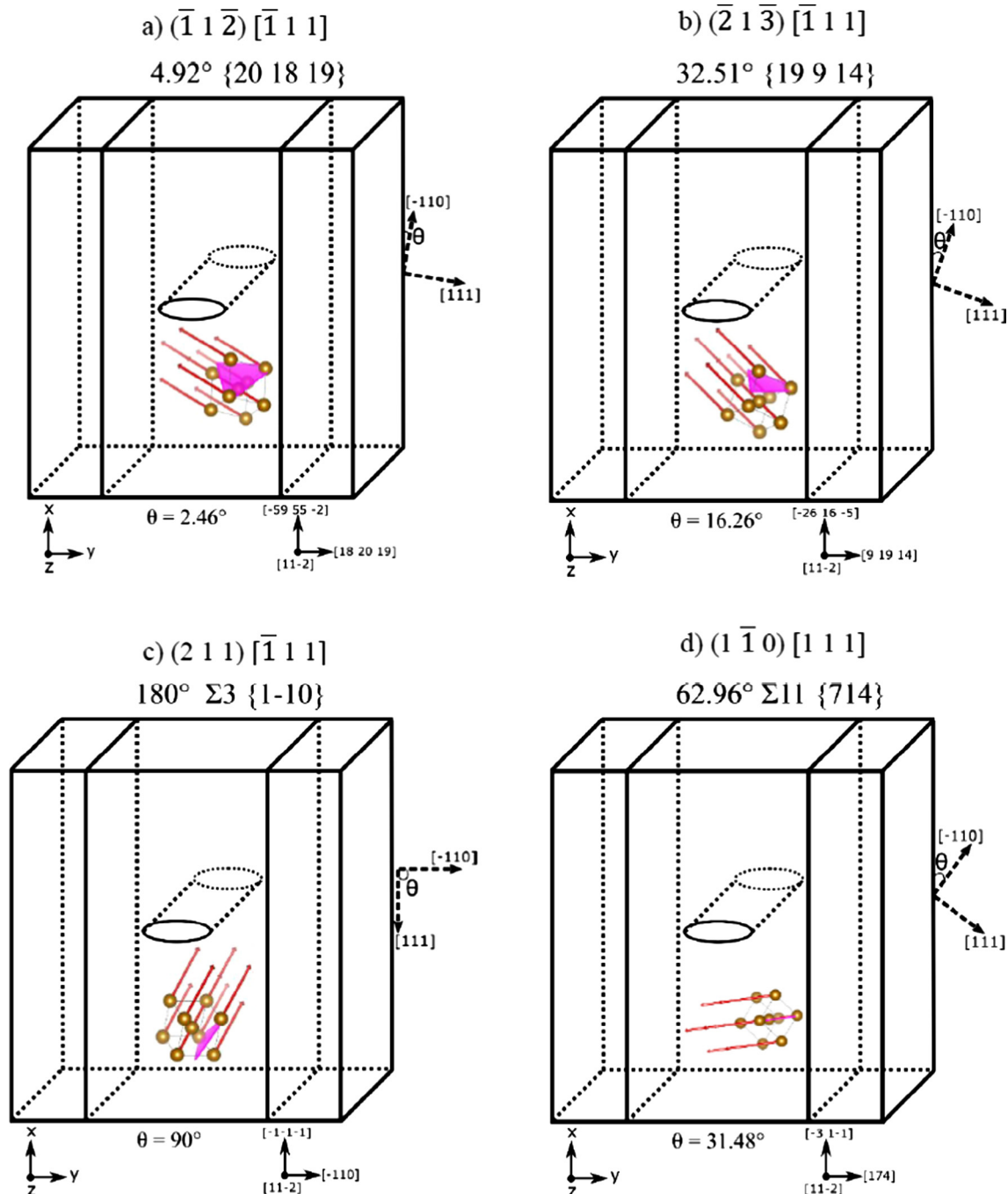


Fig. 7. Schematic of initial slip systems (pink color for plane and red color for direction) in the different grain boundary configurations with [112] tilt axis. The slip system is shown with figure labels for each image. Here, θ is half of the tilt angle which is the angle by which each crystal is rotated. The final rotated direction is shown in the side of each image. The crystallographic directions of the central crystal C-2 are shown at the bottom of each image. (For interpretation of the references to color in this figure legend, the reader is referred to the web version of this article.)

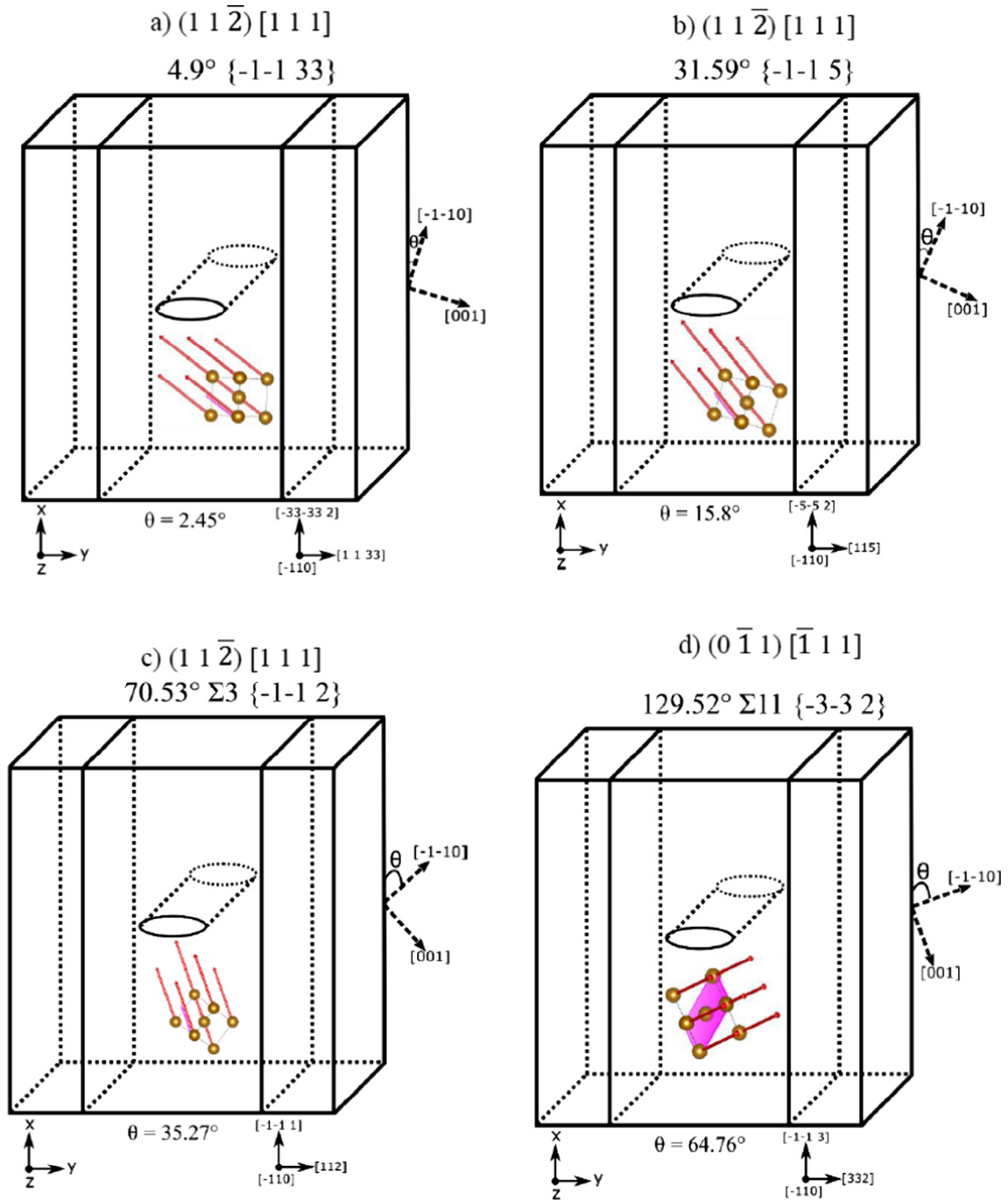


Fig. 8. Schematic of initial slip systems (pink color for plane and red color for direction) in the different grain boundary configurations with $[\bar{1}\ 1\ 0]$ tilt axis. The slip system is shown with figure labels for each image. Here, θ is half of the tilt angle which is the angle by which each crystal is rotated. The final rotated direction is shown in the side of each image. The crystallographic directions of the central crystal C-2 are shown at the bottom of each image. (For interpretation of the references to color in this figure legend, the reader is referred to the web version of this article.)

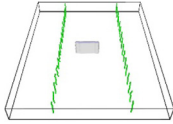
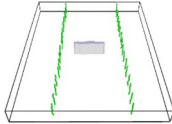
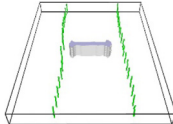
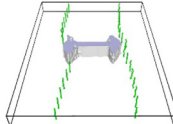
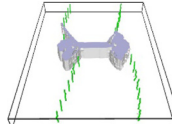
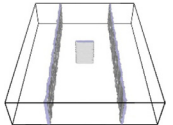
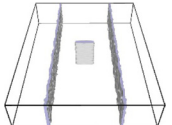
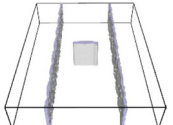
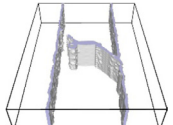
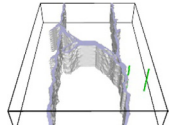
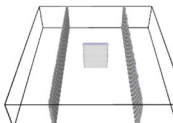
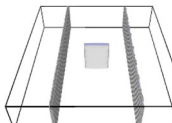
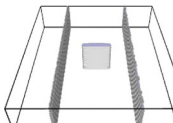
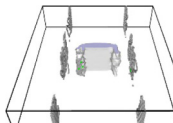
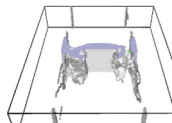
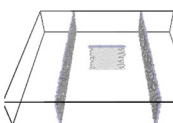
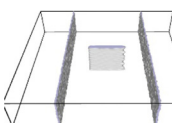
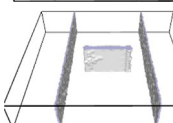
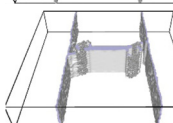
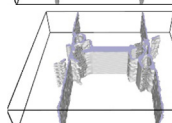
high strength. A similar variation of maximum tensile stress with grain boundary misorientation angle (tilt angle) for $[1\ \bar{1}\ 0]$ symmetric tilt grain boundaries was observed in a copper bicrystal (without crack) [18]; here too the $\Sigma 3$ boundary configuration showed a high strength.

3.4. Initial slip systems

To identify the initial active slip system in crystal C2, the slip system with the highest Schmid factor was determined for each configuration (shown in Table 1). These identified initial slip systems in the C-2 crystal were drawn using VESTA [31] and are

schematically shown in Figs. 7 and 8 for $[1\ \bar{1}\ 2]$ and $[\bar{1}\ 1\ 0]$ tilt axis, respectively. These figures also show the tilt angle of the crystal and the respective rotated crystallographic directions. It was expected that slip would initially occur on the slip system with the highest Schmid factor. The orientation of the loading direction with respect to the crystal is different in each configuration, thus the active slip systems and their corresponding Schmid factors would also differ. This could result in a difference in the nucleation of dislocations from the crack tip and their motion towards the grain boundary for each configuration. For both tilt axes cases, the general high angle grain boundary configuration had the highest Schmid factor, whereas the $\Sigma 3$ grain boundary configurations

Table 2
Snapshots of grain boundaries with $[11\bar{2}]$ tilt axis emitting dislocations at different strain. The crack is perpendicular to the grain boundary plane.

GB types	Strain				
	0.02	0.04	0.06	0.08	0.1
4.92° {201819}					
32.51° {19914}					
180° Σ3 {110}					
62.96° Σ11 {714}					

had the lowest Schmid factor = 0.314. In the $\Sigma 3$ configuration, as the occurrence of slip was difficult due to low Schmid factor, it is likely that the grain boundaries start to deform. In the 4.92° {201819} configuration, the dislocations in the grain boundary region have the slip system $(0\bar{1}1)[111]$ with a Schmid factor of 0.02. Since the Schmid factor for this slip system is less than that of the C-2 crystal, the mobility of the dislocations was less.

3.5. Visualization of dislocations and deformation twins

Using the dislocation extraction algorithm (DXA) in crystal analysis tool (CATool), dislocations and dislocation line length were extracted and the dislocations were visualized using OVITO. The snapshots at different strain are shown in [Tables 2 and 3](#). The corresponding videos are shown in [supplementary material](#). [Fig. 9](#) shows the presence of twinned regions near the crack tip. It has been reported in literature that twinning is an important deformation mechanism at the crack tip at low temperature in bcc iron for several orientations [\[32\]](#).

3.5.1. $[11\bar{2}]$ tilt axis ([Table 2](#))

The low angle grain boundary configuration 4.92° {201819} consists of dislocations of type $\frac{1}{2}\langle 111 \rangle$ (green color). On application of strain, the deformed/strained region (grey color) from the crack tip moved towards the grain boundary. The dislocations from the grain boundary showed little movement due to low Schmid factor towards the deformed/strained region. Similar observation of grain boundary movement was seen during shear deformation in fcc materials [\[22,33–36\]](#). For $\varepsilon > 0.06$, few dislocations disappeared in the strained region. See [video V1 in supplementary material](#).

For the general high angle grain boundary configuration 32.51° {19914}, strain field from the crack tip spread and interacted with the grain boundary. After that the grain boundary emitted dislocations. Frøseth et al. demonstrated the emission of dislocations from grain boundary using molecular dynamics simulation [\[35\]](#). In the current work, no dislocation was emitted from the crack tip. The strain field from the crack disturbed the grain boundary which

later emitted more dislocations. See [video V2 in supplementary material](#).

The 180° $\Sigma 3$ {110} configuration had dislocations of type $\frac{1}{2}\langle 111 \rangle$ in the grain boundary plane and parallel to the loading direction. For $\varepsilon > 0.06$, the crack emitted dislocations with Burgers vector $\frac{1}{2}[111]$ and $\frac{1}{2}[1\bar{1}\bar{1}]$ towards the boundary and the strain field of the crack tip started interacting with the grain boundary. This resulted in the atoms moving to the dislocation core thereby breaking the dislocation line leading to the collapse of the grain boundary. See [video V3 in supplementary material](#).

For the case of 62.96° $\Sigma 11$ {714} at $\varepsilon = 0.08$, dislocations of types $\frac{1}{6}\langle 111 \rangle$ and $\frac{1}{12}\langle 111 \rangle$ were emitted from the crack tip which interacted with the grain boundaries and damaged the grain boundary region. See [video V4 in supplementary material](#).

Deformation twins were seen at the crack tip in the 62.96° $\Sigma 11$ {714} and 32.51° {19914} configurations under $[11\bar{2}]$ tilt axis ([Fig. 9](#)). The interface between the twinned region and the parent were of partial dislocations of types $\frac{1}{6}\langle 111 \rangle$ and phase transformed hcp and fcc structured atoms.

3.5.2. $[\bar{1}10]$ tilt axis ([Table 3](#))

Low angle boundary 4.9° $\{\bar{1}\bar{1}33\}$ had sessile dislocations of type $\langle 100 \rangle$ (pink color) in the boundary region. At $\varepsilon = 0.06$, dislocations of type $\frac{1}{2}\langle 111 \rangle$ (green color) were emitted from the crack moving towards the low angle boundary. At $\varepsilon = 0.08$, the highly strained atoms (grey color) and $\frac{1}{2}\langle 111 \rangle$ type of dislocations from the crack interacted with the core of the dislocations in the boundary thereby breaking the dislocation line resulting in the collapse of the low angle boundary. See [video V5 in supplementary material](#).

For the general high angle boundary 31.59° $\{\bar{1}\bar{1}5\}$, at $\varepsilon = 0.06$ many dislocations of type $\langle 100 \rangle$ appeared in the grain boundary region with a simultaneous emission of $\frac{1}{2}\langle 111 \rangle$ type of dislocations from the crack tip which interacted with the grain boundary. At $\varepsilon = 0.1$, several dislocation loops were formed as a result of this interaction. Molecular dynamics simulation studies of grain boundaries in fcc nanocrystalline material, show that grain boundaries act as a source of dislocations [\[35,36\]](#). See [video V6 in supplementary material](#).

$70.53^\circ \Sigma 3 \{\bar{1}\bar{1}2\}$ is a coherent twin grain boundary and hence the boundary is not visible in OVITO visualization. After a strain of 0.04, partial dislocations of types $\frac{1}{6}\langle 111 \rangle$ and $\frac{1}{12}\langle 111 \rangle$ appeared in the coherent twin grain boundary region and moved towards the surface of the simulation box, which was similar to the observation in Ref. [37]. At $\varepsilon = 0.06$, $\frac{1}{2}\langle 111 \rangle$ type of dislocations from the crack tip moved towards the grain boundary and interacted with partial dislocations giving sessile dislocation. Jin et al. [36] simulated dislocation–coherent twin boundary interaction using molecular dynamics. They observed that both glissile and sessile dislocation can be created in the twin boundary which depends on both the type of interacting dislocation and the twin boundary. Partial dislocations of types $\frac{1}{6}\langle 111 \rangle$ and $\frac{1}{12}\langle 111 \rangle$ emitted from the crack tip moved parallel to the grain boundary without disturbing the grain boundary region, so the strength of this configuration was high (Fig. 4). See [video V7 in supplementary material](#).

In $129.52^\circ \Sigma 11 \{\bar{3}\bar{3}2\}$ configuration, partial dislocations of types $\frac{1}{6}\langle 111 \rangle$ and $\frac{1}{12}\langle 111 \rangle$ were emitted from the crack tip. These moved towards the grain boundaries and destroyed it. From that destroyed area of the grain boundary dislocations were emitted.

For the $[\bar{1}10]$ tilt axis configurations, deformation twins were observed near the crack tip in $4.9^\circ \{\bar{1}\bar{1}33\}$, $70.53^\circ \Sigma 3 \{\bar{1}\bar{1}2\}$ and $129.52^\circ \Sigma 11 \{\bar{3}\bar{3}2\}$ configurations. In the $4.9^\circ \{\bar{1}\bar{1}33\}$ configuration, multiple deformation twins were formed with fcc region at the interfaces. In $129.52^\circ \Sigma 11 \{\bar{3}\bar{3}2\}$ configuration, it was seen that the twinned region grows with increasing strain. In all cases, partial dislocations moved in the twin interface. Similar twinned regions were seen ahead of crack tip in bcc iron [38,39]. In the present study, twinning ahead of crack tip was seen to result in crack blunting, similar to the observation seen in Ref. [38].

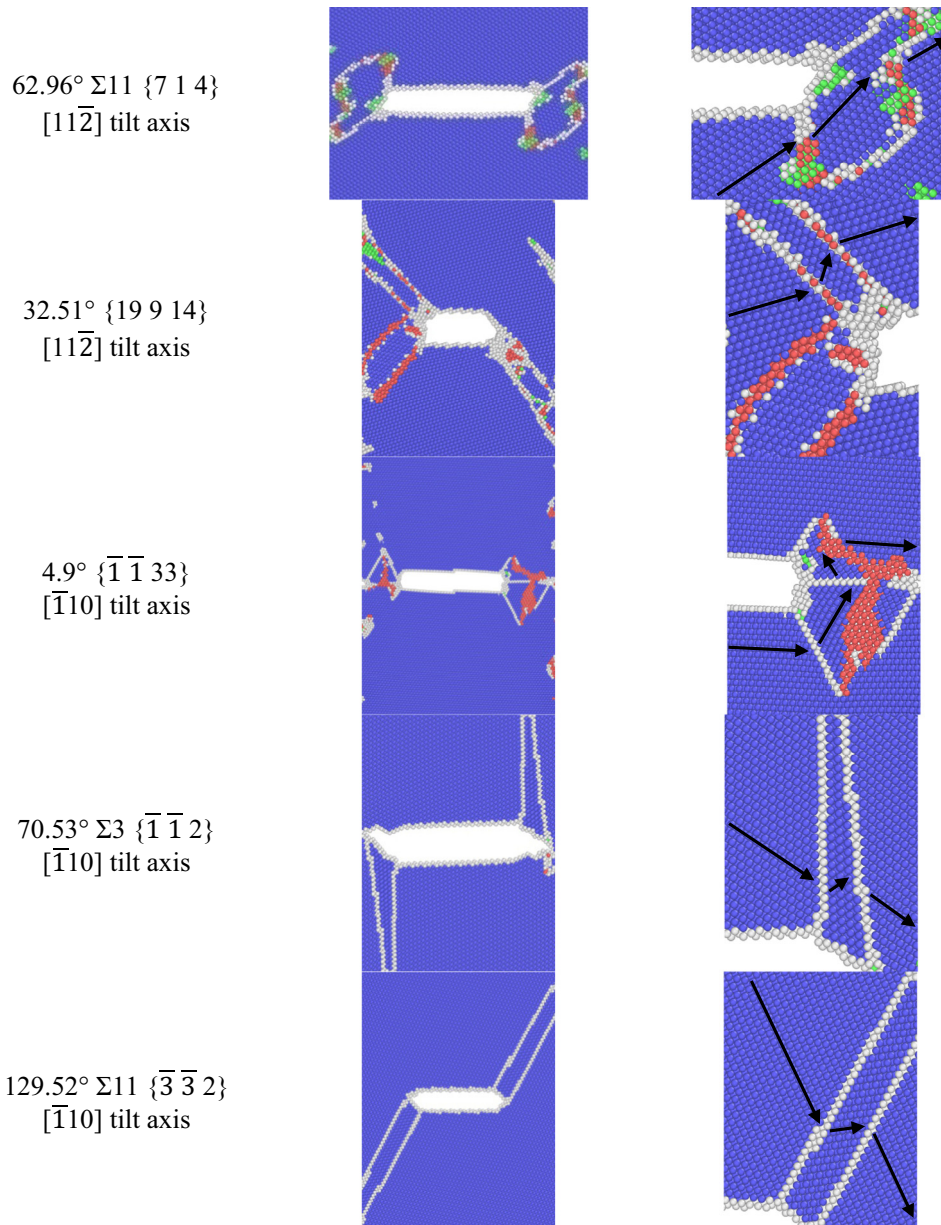


Fig. 9. Visualization of deformation twins in various grain boundary configurations mentioned on left column. The right image is a magnified view of the left image. The arrows represent a direction in the crystal and its reorientation in the twin. Bcc atoms are shown as blue, hcp atoms as red and fcc atoms as green. (For interpretation of the references to color in this figure legend, the reader is referred to the web version of this article.)

Table 3Snapshots of grain boundaries with $[\bar{1}10]$ tilt axis emitting dislocations at different strain. The crack is perpendicular to the grain boundary plane.

GB types	Strain				
	0.02	0.04	0.06	0.08	0.1
4.9° $\{\bar{1}133\}$					
31.59° $\{\bar{1}15\}$					
70.53° $\Sigma 3 \{\bar{1}12\}$					
129.52° $\Sigma 11 \{\bar{3}32\}$					

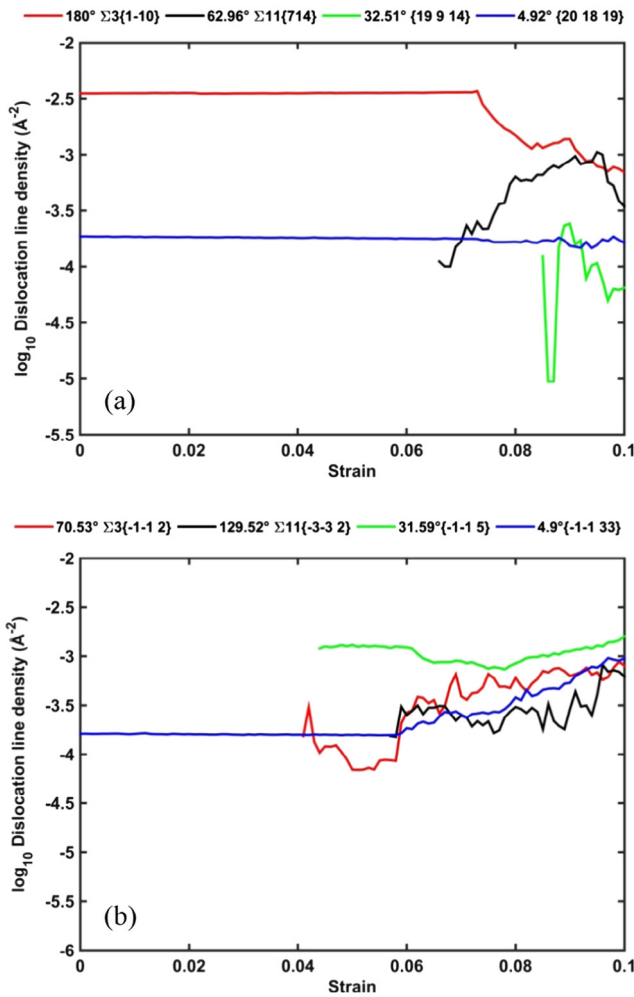


Fig. 10. Variation of dislocation line density as a function of strain for different grain boundary configurations with (a) $[11\bar{2}]$ tilt axis and (b) $[\bar{1}10]$ tilt axis.

3.6. Dislocation line density

The dislocation line density was calculated at every timestep and is shown as a function of strain in Fig. 10. The $180^\circ \Sigma 3 \{1\bar{1}0\}$ configuration contained the highest initial dislocation density because of the already existing dislocations in the grain boundary plane. With increasing strain, the grain boundary structure was disturbed by the strain field from the crack, and later by some dislocations from the crack tip. This caused the dislocation line density to decrease. The $4.92^\circ \{201819\}$ configuration also contained dislocations in the boundary to start with. With increase in strain, the dislocation line density initially decreased due to the sink of some dislocations into the highly strained field near the crack tip. Later at higher strain, dislocations were emitted from the grain boundary. The $62.96^\circ \Sigma 11 \{714\}$ and $32.51^\circ \{19914\}$ configurations did not have any dislocations to start with. With increasing strain the dislocation line density increased till 0.2 strain.

For the configurations with $[\bar{1}10]$ tilt axis, only the low angle grain boundary $4.9^\circ \{\bar{1}\bar{1}33\}$ configuration contained dislocations to start with. In this case with increasing strain, the dislocation line density increased further because of the nucleation of dislocations from the crack tip. The general high angle boundary configuration $31.59^\circ \{\bar{1}\bar{1}5\}$ contained no dislocations initially, and after a strain of 0.045 sessile dislocations of type $\langle 100 \rangle$ nucleated in the grain

boundary region. Later, these sessile dislocations interacted with themselves creating $\frac{1}{2} \langle 111 \rangle$ type of dislocations. Due to the interaction of dislocations from the crack tip the dislocation line density decreased. The $70.53^\circ \Sigma 3 \{\bar{1}\bar{1}2\}$ coherent twin grain boundary configuration contained no dislocations initially. With increasing strain dislocations nucleated from the grain boundary, moved towards the surface and disappeared resulting in the decrease of the dislocation line density. For $\varepsilon > 0.06$, more dislocations nucleated from the grain boundary and crack tip. In $129.52^\circ \Sigma 11 \{3\bar{3}2\}$ configuration, the dislocations nucleated from the crack tip, moved towards the grain boundary and disappeared there, which decreased the dislocation line density. For $\varepsilon > 0.08$, partial dislocations nucleated within the grain boundary and emitted from the damaged region of the grain boundary resulting in an increased dislocation line density.

From the above results, it is seen that for $\varepsilon > 0.08$, the high angle grain boundaries $32.51^\circ \{19914\}$ and $31.59^\circ \{\bar{1}\bar{1}5\}$ emitted $\frac{1}{2} \langle 111 \rangle$ type of perfect dislocations and the $\Sigma 11$ grain boundaries $62.96^\circ \Sigma 11 \{714\}$ and $129.52^\circ \Sigma 11 \{3\bar{3}2\}$ emitted partial dislocations. Studies in literature too show that the type of dislocation emitted from the grain boundary depends on the structural character of the grain boundary [23].

3.7. Stress screening effect

During deformation, grain boundaries may screen the stress field from the crack tip as mentioned in Section 2.4. Figs. 11 and 12 shows the ratios of stresses for different grain boundary configurations with $[11\bar{2}]$ and $[\bar{1}10]$ tilt axis respectively. The ratios of the stresses near the grain boundary to that near the crack tip in both the configurations with and without the grain boundary are given by $\frac{\sigma_b}{\sigma_a}$ and $\frac{\sigma_b'}{\sigma_a'}$ respectively. If the ratio is equal to one, the stresses in C-1 near the grain boundary and in C-2 near the crack tip are same. Deviation from that value gives an outlook of the stress screening property of the grain boundary. Screening happens when both $\frac{\sigma_b}{\sigma_a} < 1$ and $\frac{\sigma_b}{\sigma_a} < \frac{\sigma_b'}{\sigma_a'}$. In $[11\bar{2}]$ tilt axis case, $32.5^\circ \{19914\}$ and $62.96^\circ \Sigma 11 \{714\}$ configurations showed stress screening till 0.05 strain. At higher strain, the grain boundary region got damaged due to the strain field from the crack tip. In $[\bar{1}10]$ tilt axis, effective stress screening was observed in $4.9^\circ \{\bar{1}\bar{1}33\}$ and $31.59^\circ \{\bar{1}\bar{1}5\}$ configurations. Comparing all configurations from both the tilt axes and looking at initial strain ($\varepsilon < 0.05$), the $31.59^\circ \{\bar{1}\bar{1}5\}$ and $4.9^\circ \{\bar{1}\bar{1}33\}$ configurations had the highest stress screening effect, followed by $62.96^\circ \Sigma 11 \{714\}$ and then $32.5^\circ \{19914\}$.

4. Discussion

In this article, the interaction of a crack with four different grain boundaries – $\Sigma 3$, $\Sigma 11$, a low angle boundary and a general high angle boundary was studied. Each of these boundaries was constructed using two different tilt axis $[11\bar{2}]$ and $[\bar{1}10]$ to compare the effect of the tilt axis on the strength of the configuration. The grain boundaries were equilibrated to get a minimum grain boundary energy configuration after which a crack was introduced at the centre lying perpendicular to the boundaries. Similar molecular dynamics simulations of crack interaction with single crystal iron [32], α/γ phase boundaries [40], polycrystalline iron [20] and with stable and unstable grain boundaries [41] under mode I and cyclic loading [21] conditions have been studied earlier. Molecular dynamics simulation of deformation of polycrystalline molybdenum [42] showed the formation of cracks at grain boundaries. Similar to the present work, there were studies carried out with a brittle crack in configurations with low angle and high angle grain

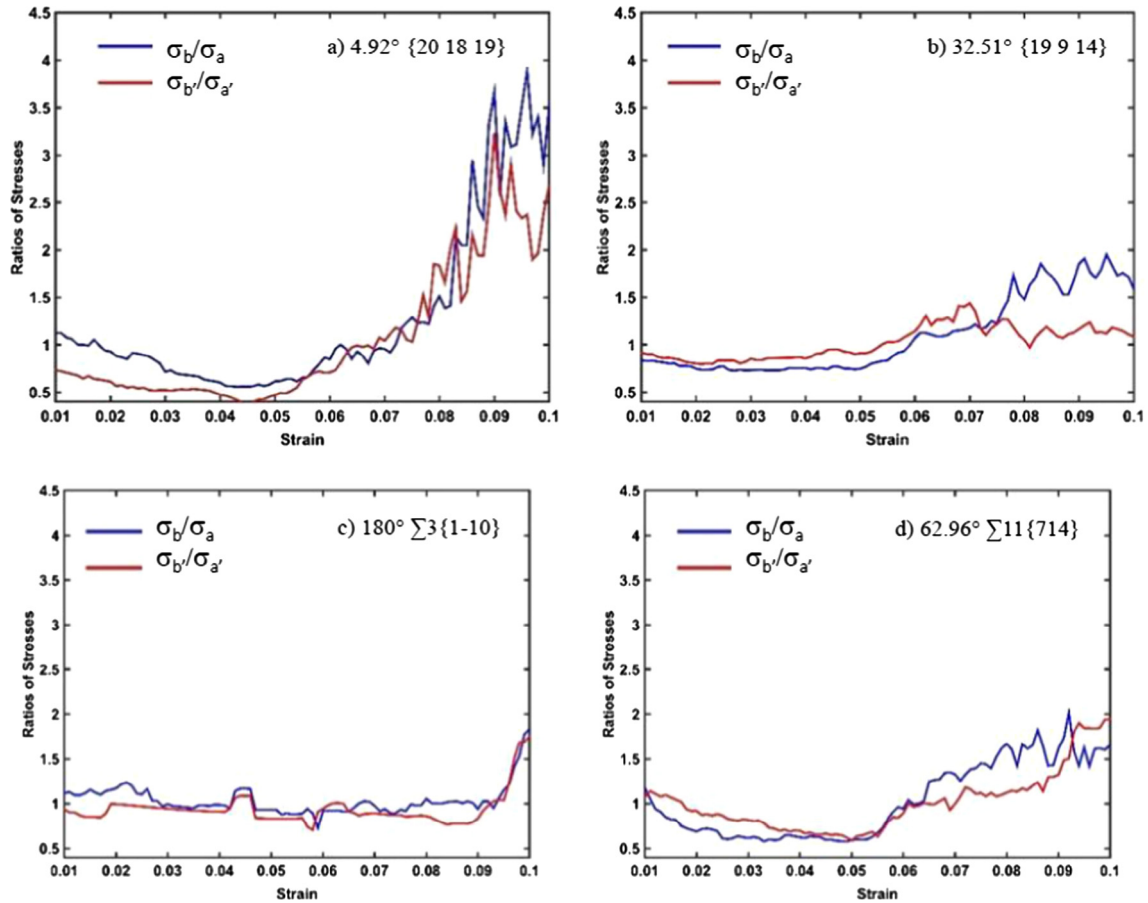


Fig. 11. Ratios of stresses as a function of strain for grain boundaries with $[1\bar{1}2]$ tilt axis (a) $4.92^\circ \{20\ 18\ 19\}$, (b) $32.51^\circ \{19\ 9\ 14\}$, (c) $180^\circ \Sigma 3 \{1\bar{1}0\}$, (d) $62.96^\circ \Sigma 11 \{714\}$. σ_a - stress near crack tip in grain boundary system; σ_b - stress near grain boundary in grain boundary system; σ_a' - stress near crack tip in single crystal; σ_b' - stress away from crack in single crystal.

boundaries with $\langle 1\ 0\ 0 \rangle$ tilt axis [38] and with different crack orientation in $\Sigma 3$ $\{112\}$ coherent twin boundary in bcc iron [39]. In the present work, only the initial part (dislocation emission from crack/grain boundary) of the interaction between the nano-crack and the different grain boundaries was shown, with the aim to compare the different configurations. Thus, as compared to previous studies the present work gives a detailed analysis of initial crack interaction with different grain boundaries.

Of the various grain boundaries found in a metal, the $\Sigma 3$ boundaries are special as they have a high misorientation angle but low grain boundary energy. Of the two $\Sigma 3$ boundaries considered in this study, one was $180^\circ \Sigma 3 \{1\bar{1}0\}$ about $[1\bar{1}2]$ tilt axis and the other was $70.53^\circ \Sigma 3 \{\bar{1}\bar{1}2\}$ about $[\bar{1}10]$ tilt axis. The former is an incoherent CSL boundary and the later is a coherent CSL boundary. $180^\circ \Sigma 3 \{1\bar{1}0\}$ contained $\frac{1}{2} \langle 1\ 1\ 1 \rangle$ type of dislocations in the grain boundary region and had a grain boundary energy of 373.56 mJ/m^2 . The maximum tensile stress of this configuration (grain boundary and crack) was 20 GPa. $70.53^\circ \Sigma 3 \{\bar{1}\bar{1}2\}$ being a coherent twin grain boundary contained no dislocations in it and had a grain boundary energy of 291.4 mJ/m^2 . The maximum tensile stress of this configuration was 20.9 GPa. In both the $\Sigma 3$ boundary configurations, the slip system in C2 crystal had low a Schmid factor suggesting the lack of favourable slip systems in crystal C2. Further, as the dislocations present in the $180^\circ \Sigma 3 \{1\bar{1}0\}$ grain boundary configuration were of the $\frac{1}{2} \langle 1\ 1\ 1 \rangle$ type and were parallel to the loading direction, their Schmid factor was zero. In the coherent twin grain boundary $70.53^\circ \Sigma 3 \{\bar{1}\bar{1}2\}$ configuration,

during deformation the dislocations originated in the grain boundary region because the Schmid factor for slip systems in crystal C2 were low. High stability and low Schmid factor of the $\Sigma 3$ grain boundaries made these configurations difficult to deform thus giving high maximum tensile stress values. Frøseth et al. discussed about the stability of CSL grain boundaries during uniaxial constant-stress deformation simulations [43]. In low grain boundary energy configurations, nucleation of any defect is difficult making them stable boundary configurations. Liu et. al. observed crack tip interaction with coherent twin boundaries (CTB) in copper under high resolution transmission electron microscope (HRTEM) and also with molecular dynamics simulation [16]. They found that partial dislocations activated in the CTB region enhanced the strength. This same phenomenon was also observed in the present study in $70.53^\circ \Sigma 3 \{\bar{1}\bar{1}2\}$ coherent twin boundary.

Low angle boundaries are walls of dislocations commonly observed in deformed materials where geometrically necessary dislocations rearrange to form cells and sub-grains with low angle of misorientation across them. In the present study, configurations $4.92^\circ \{201819\}$ and $4.9^\circ \{\bar{1}\bar{1}33\}$ contain dislocations of types $\frac{1}{2} \langle 1\ 1\ 1 \rangle$ (glissile) and $\langle 1\ 0\ 0 \rangle$ (sessile) respectively in their grain boundary regions. The slip system of the glissile dislocations in $4.92^\circ \{201819\}$ has a very low Schmid factor (0.02) and hence the dislocations do not move on the application of tensile load. Crystal C-2 contains slip system with a high Schmid factor (0.479) resulting in dislocations moving from crack tip towards grain boundary. The $4.9^\circ \{\bar{1}\bar{1}33\}$ boundary had $\langle 1\ 0\ 0 \rangle$ sessile

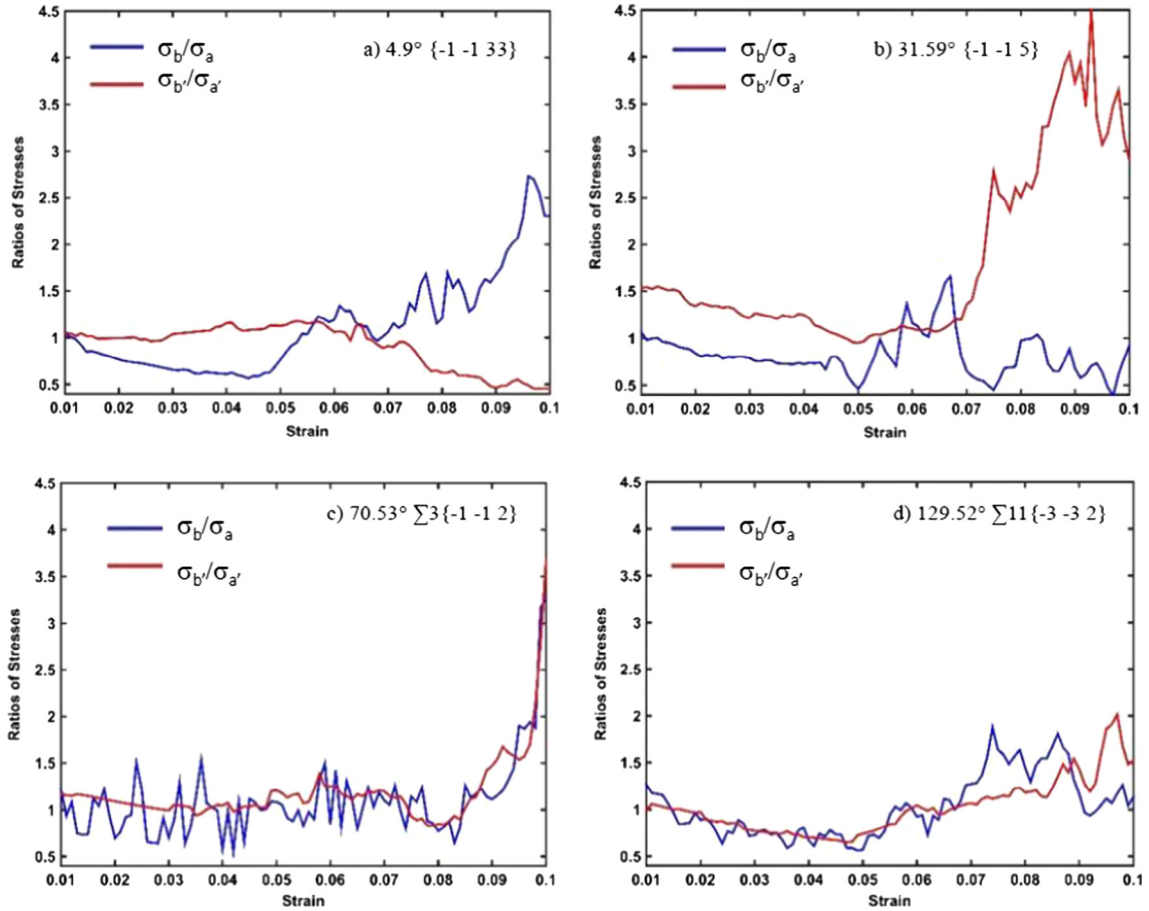


Fig. 12. Ratios of stresses as a function of strain for grain boundaries with $[\bar{1}10]$ tilt axis (a) $4.9^\circ \{\bar{1}\bar{1}33\}$, (b) $31.59^\circ \{\bar{1}\bar{1}5\}$, (c) $70.53^\circ \Sigma 3 \{\bar{1}\bar{1}2\}$, (d) $129.52^\circ \Sigma 11 \{-3-32\}$. σ_a - stress near crack tip in grain boundary system; σ_b - stress near grain boundary in grain boundary system; σ_a' - stress near crack tip in single crystal; σ_b' - stress away from crack in single crystal.

dislocations which get destroyed after interaction with the dislocations from the crack tip thereby making this configuration weaker than 4.92° [201819]. In the low angle boundary configurations, the dislocations in the grain boundary regions (Tables 2 and 3) were either glissile with low Schmid factor or sessile dislocations making the grain boundary region stronger and so the configurations showed higher maximum tensile strength.

General high angle grain boundaries are configurations with high tilt angle and high grain boundary energy. Deforming the $31.59^\circ \{\bar{1}\bar{1}5\}$ configuration resulted in the creation of $\langle 100 \rangle$ type of dislocations in the grain boundary region which increased the tensile strength of the grain boundary. Similarly, Zhang et al. [18] observed the nucleation of partial dislocations from 38.9° symmetric tilt grain boundary under tensile loading. In 32.51° [19914] configuration, no dislocation was emitted from the crack tip, but the strain field from the crack destroyed the grain boundary.

$\Sigma 11$ grain boundaries are high angle grain boundaries with lower grain boundary energy. In configurations with $\Sigma 11$ boundaries of both the tilt axes, partial dislocations were emitted from the crack tip towards the grain boundary. The high angle and $\Sigma 11$ grain boundaries not only acted as dislocation sinks, but also as dislocation sources at higher strain $\epsilon > 0.08$. Similar observations of dislocation sink and emission in the grain boundary region were found using molecular dynamic simulation in nanocrystalline Au [24].

From simulations carried out on configurations with only crack but no boundaries, it was seen that the presence of grain boundaries did not increase the strength of the material. Single crystal configurations showed marginally higher maximum tensile stress

than that with grain boundaries, for the same orientations. It was seen that dislocations from the crack tip interacted with the grain boundary and destroyed a part of the grain boundary region which resulted in the reduction of strength. The yield stress from the current molecular dynamics simulation is higher than the experimental values, possibly due to the defect free, customized grain boundary-crack model and the specific loading direction used [44]. The decrease in tensile stress beyond the maximum value observed in this study was also seen in Ref. [18], which was attributed to the damage of the grain boundary region. The strength of the $[11\bar{2}]$ tilt axis grain boundaries were in the order: low angle GB $\approx \Sigma 3 >$ high angle GB $> \Sigma 11$ and that of the $[\bar{1}\bar{1}0]$ tilt axis grain boundaries were in the order: $\Sigma 3 >$ high angle GB \approx low angle GB $> \Sigma 11$. It was seen that both $\Sigma 3$ grain boundaries have higher strength due to their comparative low grain boundary energy [43,45], low Schmid factor for slip systems in the C2 crystal and for the dislocations in the grain boundary region. Low strength of $\Sigma 11$ grain boundaries were due to the damage in the grain boundary due to the partial dislocations from the crack tip. Tensile loading of $[\bar{1}\bar{1}0]$ symmetric tilt grain boundaries in copper using molecular dynamics showed dislocations being emitted from the grain boundary [18]. The variation of maximum tensile stress as a function of grain boundary misorientation angle [18] was similar to that of the considered $[\bar{1}10]$ tilt axis grain boundaries with crack.

The ability of a grain boundary to screen the stress field from a crack to the other side of the boundary has not been studied earlier. Low angle boundary configuration $4.9^\circ \{\bar{1}\bar{1}33\}$ showed stress

screening whereas $4.92^\circ \{201819\}$ did not. This could possibly be due to the presence of sessile dislocations in the former as compared to glissile dislocations in the later which moved from the grain boundary region. Further it was also seen from the visualization that in $4.9^\circ \{\bar{1}\bar{1}33\}$ the strain region from the crack tip moved at an angle to the grain boundary and did not affect the grain boundary region in the crack plane. Apart from $4.9^\circ \{\bar{1}\bar{1}33\}$ configuration, $31.59^\circ \{\bar{1}\bar{1}5\}$ configuration also showed an effective stress screening because of the formation of partial dislocations of type $\langle 100 \rangle$ in the grain boundary region.

5. Conclusion

- The configurations with $\Sigma 3$ grain boundaries (coherent in $[\bar{1}10]$ tilt axis and incoherent in $[11\bar{2}]$ tilt axis) had higher tensile strength than other simulated grain boundary configurations.
- Out of the eight studied configurations, those with $\Sigma 11$ boundaries had low tensile strength.
- Twin formation ahead of crack tip was observed for $62.96^\circ \Sigma 11 \{714\}$ and $32.51^\circ \{19914\}$ configurations with $[11\bar{2}]$ tilt axis, and $4.9^\circ \{\bar{1}\bar{1}33\}$, $70.53^\circ \Sigma 3 \{\bar{1}\bar{1}2\}$ and $129.52^\circ \Sigma 11 \{\bar{3}\bar{3}2\}$ configurations with $[\bar{1}10]$ tilt axis.

- General high angle and $\Sigma 11$ grain boundaries act initially as dislocation sinks and later as dislocation sources.
- The structure of the grain boundary controls the type of the dislocations emitting from the grain boundary.
- At large strain, the dislocation line density was higher in $\{1\bar{1}0\}$ as compared to $\{\bar{1}\bar{1}2\}$ tilt axis configurations.
- $4.9^\circ \{\bar{1}\bar{1}33\}$ and $31.59^\circ \{\bar{1}\bar{1}5\}$ showed effective stress screening due to $\langle 100 \rangle$ type of sessile dislocations in the grain boundary region.

Acknowledgement

The authors acknowledge Naisheel Verdhhan, Ram Pradaap Singh, Ajay Revelly, Bharat Reddy and Apu Sarkar for their valuable discussions. This work was carried out under the DGFS scheme between BARC and IIT-Bombay.

Appendix A

See [Tables A1 and A2](#).

Table A1

Grain boundary energy and the maximum tensile stress of different grain boundary configurations with $[11\bar{2}]$ tilt axis.

S. no.	Σ {hkl}	Tilt angle (degrees)	GB energy (mj/m ²)	Max. tensile stress (GPa)
1	{201819}	4.92	557.60	20.9
2	$\Sigma 3 \{1\bar{1}0\}$	180	373.56	20
3	$\Sigma 5 \{5\bar{1}2\}$	101.54	1376.11	14.6
4	$\Sigma 7 \{4\bar{2}1\}$	135.58	1482.90	17.2
5	$\Sigma 11 \{714\}$	62.96	646.45	12.5
6	$\Sigma 15 \{201\}$	78.46	1551.49	13.5
7	$\Sigma 21 \{312\}$	44.42	1157.94	14.0
8	$\Sigma 25\{751\}$	156.93	1448.11	19.6
9	$\Sigma 29\{1172\}$	149.55	1512.76	18.8
10	$\Sigma 31\{825\}$	52.20	1125.66	11.4
11	$\Sigma 33 \{311\}$	117.04	1524.88	15.1
12	$\Sigma 35\{1158\}$	34.05	1104.48	15.2
13	$\Sigma 35 \{1354\}$	122.88	1428.91	16.1
14	$\Sigma 49 \{11\bar{1}5\}$	88.83	1607.62	14.5
15	$\Sigma 53\{13710\}$	27.53	1294.77	14.8
16	{19914}	32.51	1405.45	16.2
17	{11910}	9.34	789.28	17.6
18	{867}	13.31	937.99	18.7

Table A2

Grain boundary energy and the maximum tensile stress of different grain boundary configurations with $[\bar{1}10]$ tilt axis.

S. no.	Σ {hkl}	Tilt angle (degrees)	GB energy (mj/m ²)	Max. tensile stress (GPa)
1	$\{\bar{1}\bar{1}33\}$	4.91	643.38	15.3
2	$\Sigma 3 \{\bar{1}\bar{1}1\}$	109.47	1521.77	13.4
3	$\Sigma 3 \{\bar{1}\bar{1}2\}$	70.53	291.41	20.9
4	$\Sigma 9 \{\bar{2}\bar{2}1\}$	141.06	1481.29	8.2
5	$\Sigma 9 \{\bar{1}\bar{1}4\}$	38.94	1397.37	16.8
6	$\Sigma 11 \{\bar{3}\bar{3}2\}$	129.52	1207.83	9.7
7	$\Sigma 11 \{\bar{1}\bar{1}3\}$	50.48	1351.69	17.4
8	$\Sigma 17 \{\bar{2}\bar{2}3\}$	86.63	1273.53	17.4
9	$\Sigma 17 \{\bar{3}\bar{3}4\}$	93.37	1375.55	19.1
10	$\Sigma 19 \{\bar{3}\bar{3}1\}$	153.47	1561.88	7.1
11	$\Sigma 19 \{\bar{1}\bar{1}6\}$	26.53	1410.21	15.6
12	$\Sigma 27 \{\bar{5}\bar{5}2\}$	148.41	1489.07	7.5
13	$\Sigma 27 \{\bar{1}\bar{1}5\}$	31.59	1470.44	15.8
14	$\Sigma 33 \{\bar{4}\bar{4}1\}$	159.95	1447.09	6.7
15	$\Sigma 33 \{\bar{5}\bar{5}4\}$	121.01	1366.15	11.0
16	$\Sigma 33 \{\bar{2}\bar{2}5\}$	58.99	1130.34	18.9
17	$\Sigma 33 \{\bar{1}\bar{1}8\}$	20.05	1334.97	14.6
18	$\Sigma 99 \{\bar{1}\bar{1}14\}$	11.54	1062.76	14.8
19	$\Sigma 99 \{\bar{1}\bar{1}20\}$	8.09	881.38	15.2

Appendix B. Supplementary material

Supplementary data associated with this article can be found, in the online version, at <http://dx.doi.org/10.1016/j.commatsci.2017.05.026>.

References

- [1] P. Lejcek, Grain Boundary Segregation in Metals, 2010.
- [2] D. Wolf, Correlation between the energy and structure of grain boundaries in b.c.c. metals I. Symmetrical boundaries on the (110) and (100) planes, *Philos. Mag. Part B* 59 (January 2015) (1989) 667–680.
- [3] D. Wolf, Correlation between the energy and structure of grain boundaries in b.c.c. metals. II. Symmetrical tilt boundaries, *Philos. Mag. A* 62 (January 2015) (1990) 447–464.
- [4] R.E. Rudd, Void growth in BCC metals simulated with molecular dynamics using the finnis-sinclair potential, *Philos. Mag.* 89 (December) (2009) 3133–3161, 34–36.
- [5] K. Tohgo, H. Suzuki, Y. Shimamura, G. Nakayama, T. Hirano, Monte Carlo simulation of stress corrosion cracking on a smooth surface of sensitized stainless steel type 304, *Corros. Sci.* 51 (9) (2009) 2208–2217.
- [6] M. Marx, W. Schaefer, H. Vehoff, Interaction of short cracks with the local microstructure, *Proc. Eng.* 2 (1) (2010) 163–171.
- [7] A. Brückner-Foit, X. Huang, Numerical simulation of micro-crack initiation of martensitic steel under fatigue loading, *Int. J. Fatigue* 28 (2006) 963–971.
- [8] W. Schaefer, M. Marx, A numerical description of short fatigue cracks interacting with grain boundaries, *Acta Mater.* 60 (5) (2012) 2425–2436.
- [9] W. Ludwig, J.Y. Buffière, S. Savelli, P. Cloetens, Study of the interaction of a short fatigue crack with grain boundaries in a cast Al alloy using X-ray microtomography, *Acta Mater.* 51 (2003) 585–598.
- [10] H. Van Swygenhoven, Polycrystalline materials: Grain boundaries and dislocations, *Science* (80-) 296 (April) (2002) 66–68.
- [11] S. Taira, K. Tanaka, Y. Nakai, A model of crack-tip slip band blocked by grain boundary, *Mech. Res. Commun.* 5 (6) (1978) 375–381.
- [12] P.D. Zavattieri, H.D. Espinosa, Grain level analysis of crack initiation and propagation in brittle materials, *Acta Mater.* 49 (2001) 4291–4311.
- [13] K. Tanaka, Y. Akinawa, Y. Nakai, R.P. Wei, Modeling of small fatigue crack-growth interacting with grain-boundary, *Eng. Fract. Mech.* 24 (6) (1986) 803–819.
- [14] S.H. Hideyuki Inoue, Yasuhiro Akahoshi, Molecular dynamics simulation on fracture mechanisms of nano-scale polycrystal under static and cyclic loading, *Mater. Sci. Res. Int.* 1 (2) (1995) 95–99.
- [15] A. Yu, N. Andrey, Molecular dynamics study of behavior of symmetrical tilt grain boundaries in BCC and FCC metals under shear loading, in: *Proc. XLII Int. Summer Sch. APM 2014*, vol. 9(122), 2014, pp. 50–57.
- [16] L. Liu, J. Wang, S.K. Gong, S.X. Mao, Atomistic observation of a crack tip approaching coherent twin boundaries, *Sci. Rep.* 4 (2014) 4397.
- [17] R.M. Lynden-Bell, A simulation study of induced disorder, failure and fracture of perfect metal crystals under uniaxial tension, *J. Phys. Condens. Matter* 7 (24) (1995) 4603.
- [18] L. Zhang, C. Lu, K. Tieu, L. Pei, X. Zhao, K. Cheng, Molecular dynamics study on the grain boundary dislocation source in nanocrystalline copper under tensile loading, *Mater. Res. Exp.* 2 (3) (2015) 35009.
- [19] W.-J. Chang, Molecular-dynamics study of mechanical properties of nanoscale copper with vacancies under static and cyclic loading, *Microelectron. Eng.* 65 (1–2) (2003) 239–246.
- [20] A. Latapie, D. Farkas, Molecular dynamics investigation of the fracture behavior of nanocrystalline α -Fe, *Phys. Rev. B* 69 (13) (2004) 1–9.
- [21] K. Nishimura, N. Miyazaki, Molecular dynamics simulation of crack growth under cyclic loading, *Comput. Mater. Sci.* 31 (2004) 269–278.
- [22] Y. Mishin, M. Winning, G. Gottstein, L.S. Shvindlerman, Stress-induced grain boundary migration, *Acta Mater.* 49 (2) (2001) 211–219.
- [23] D.E. Spearot, M.A. Tschopp, K.I. Jacob, D.L. McDowell, Tensile strength of (100) and (110) tilt bicrystal copper interfaces, *Acta Mater.* 55 (2) (2007) 705–714.
- [24] A. Hasnaoui, P.M. Derlet, H. Van Swygenhoven, Interaction between dislocations and grain boundaries under an indenter - a molecular dynamics simulation, *Acta Mater.* 52 (8) (2004) 2251–2258.
- [25] S. Ranganathan, On the geometry of coincidence-site lattices, *Acta Crystallogr.* 21 (2) (1966) 197–199.
- [26] S. Plimpton, Fast parallel algorithms for short-range molecular dynamics, *J. Comput. Phys.* 117 (1) (1995) 1–19.
- [27] M.A. Tschopp, D.L. McDowell, Structures and energies of Σ 3 asymmetric tilt grain boundaries in copper and aluminium, *Philos. Mag.* 87 (22) (2007) 3147–3173.
- [28] G.J. Ackland, D.J. Bacon, A.F. Calder, T. Harry, Computer simulation of point defect properties in dilute Fe–Cu alloy using a many-body interatomic potential, *Philos. Mag. A* 75 (3) (1997) 713–732.
- [29] A. Stukowski, Visualization and analysis of atomistic simulation data with OVITO—the Open Visualization Tool, *Model. Simul. Mater. Sci. Eng.* 18 (1) (2010) 15012.
- [30] A. Stukowski, K. Albe, Extracting dislocations and non-dislocation crystal defects from atomistic simulation data, *Model. Simul. Mater. Sci. Eng.* 18 (8) (2010) 85001.
- [31] K. Momma, F. Izumi, VESTA 3 for three-dimensional visualization of crystal, volumetric and morphology data, *J. Appl. Crystallogr.* 44 (6) (2011) 1272–1276.
- [32] D. Farkas, Twinning and recrystallisation as crack tip deformation mechanisms during fracture, *Philos. Mag.* 85 (2–3) (2005) 387–397.
- [33] M. Winning, Motion of (100) tilt grain boundaries, *Acta Mater.* 51 (20) (2003) 6465–6475.
- [34] M. Winning, A.D. Rollett, Transition between low and high angle grain boundaries, *Acta Mater.* 53 (10) (2005) 2901–2907.
- [35] A.G. Frøseth, P.M. Derlet, H. Van Swygenhoven, Dislocations emitted from nanocrystalline grain boundaries: nucleation and splitting distance, *Acta Mater.* 52 (20) (2004) 5863–5870.
- [36] Z.H. Jin, P. Gumbsch, K. Albe, E. Ma, K. Lu, H. Gleiter, H. Hahn, Interactions between non-screw lattice dislocations and coherent twin boundaries in face-centered cubic metals, *Acta Mater.* 56 (5) (2008) 1126–1135.
- [37] N. Li, J. Wang, A. Misra, X. Zhang, J.Y. Huang, J.P. Hirth, Twinning dislocation multiplication at a coherent twin boundary, *Acta Mater.* 59 (15) (2011) 5989–5996.
- [38] D. Terentyev, F. Gao, Blunting of a brittle crack at grain boundaries: an atomistic study in BCC Iron, *Mater. Sci. Eng. A* 576 (2013) 231–238.
- [39] G. Sainath, B.K. Choudhary, Directional anisotropy of crack propagation along Σ 3 grain boundary in BCC Fe, *Trans. Indian Inst. Met.* 69 (2) (2016) 525–530.
- [40] Y. Zhang, F.C. Zhang, L. Qian, T.S. Wang, Atomic-scale simulation of α/γ -iron phase boundary affecting crack propagation using molecular dynamics method, *Comput. Mater. Sci.* 50 (5) (2011) 1754–1762.
- [41] K. Nishimura, N. Miyazaki, Molecular dynamics simulation of crack propagation in polycrystalline material, *Comput. Model. Eng. Sci.* 2 (2) (2001) 143–154.
- [42] S.L. Frederiksen, K.W. Jacobsen, J. Schiøtz, Simulations of intergranular fracture in nanocrystalline molybdenum, *Acta Mater.* 52 (17) (2004) 5019–5029.
- [43] A.G. Frøseth, H. Van Swygenhoven, P.M. Derlet, Developing realistic grain boundary networks for use in molecular dynamics simulations, *Acta Mater.* 53 (18) (2005) 4847–4856.
- [44] D.K. Ward, W.A. Curtin, Y. Qi, Mechanical behavior of aluminum-silicon nanocomposites: a molecular dynamics study, *Acta Mater.* 54 (17) (2006) 4441–4451.
- [45] A. Hasnaoui, H. Van Swygenhoven, P.M. Derlet, On non-equilibrium grain boundaries and their effect on thermal and mechanical behaviour: a molecular dynamics computer simulation, *Acta Mater.* 50 (15) (2002) 3927–3939.